



## EXPERIMENTAL STUDY OF THE 3-D TURBULENT VELOCITY FIELD DOWNSTREAM A BLUFF BODY

**Juan José Cruz Villanueva**

**Luís Fernando Figueira da Silva**

Departamento de Engenharia Mecânica

Pontifícia Universidade Católica do Rio de Janeiro – PUC-Rio

Rua Marquês de São Vicente, 225, Gávea – Rio de Janeiro, RJ – Brasil – 3527-1176

juancruz@aluno.puc-rio.br – luisfer@esp.puc-rio.br

**Abstract.** An experimental characterization of the flow structure formed downstream of a vertically mounted bluff body is performed for three turbulent annular flows of air with Reynolds number  $Re=15000$ ,  $30000$  and  $44000$ . Three components of instantaneous velocity field are measured, using the stereo PIV technique, at the symmetry plane. The average velocity gradients and the turbulent properties are analyzed. The results show a recirculation zone consisting of a toroidal vortex, with similar dimensions for all Reynolds number. The larger turbulent fluctuations are found in the vortex region, which imply the observed anisotropy of the Reynolds stresses. Also, an analysis of the anisotropic of Reynolds tensor using the Lumley triangle is performed, revealing that the flow is generally anisotropic.

**Keywords:** experimental study; particle imaging velocimetry; Reynolds stress tensor.

### 1. INTRODUCTION

Turbulent flows downstream bluff bodies, such as cylinders or circular discs, are widely employed in industrial situations due to formation of a recirculation zone at the vicinity of the obstacle face. This recirculation arises due to the pressure drop at the near wake region, close the face of the bluff body. In this region fluctuating velocity and high strain rates fields are generated. The description of the properties at the turbulent wake region, in particular those controlled by the formation of large scale structures, is essential to an adequate understanding of the physical mechanisms which govern the flow downstream of these obstacles. This understanding is a prerequisite to develop turbulence models (Braza, *et al.*, 2006), and to describe their interactions with combustion processes.

Laser Doppler Anemometry (LDA) has been used to measure the velocity field, turbulent properties and probability density distribution in the region of recirculating annular jets for different Reynolds numbers  $Re = 0.86 - 3.6 \times 10^4$  (Duraó and Whitelaw, 1978). The turbulent fields studied resulted substantially anisotropic with minimum turbulent intensity minimum around 30%.

The evolution of the shear layer issuing from the edge of a circular bluff body has been studied (Huang and Lin, 2000) for Reynolds numbers up to  $2.0 \times 10^3$ . Concerning the flow structure five characteristic modes have been found: laminar, subcritical, transitional, supercritical and turbulent. In these cases, flow, patterns vortex radius length and turbulent properties have been shown to be closely related to the characteristic modes, although slight variations in the position of the center and radius of the vortex have been found for the supercritical and turbulent modes. More recently, high-repetition-rate PIV measurements have been made in a wind tunnel to study annular recirculation region (Kähler, 2011). The temporal analysis of the wake frequency spectrum indicated that periodic vortex shedding is absent. Results also show that tracer particles with diameter smaller than  $1 \mu m$  are suitable for the characterization of the near wall region and wake region dynamic structure.

This study aims to describe the turbulent flow properties and structure of the recirculation region downstream to a bluff body of simple cylindrical geometry. This is significant to combustion applications, since it is capable to stabilize non premixed flames at the recirculation zone. Also, access to all combustion regimes (laminar to extinction) is possible, including flamelet and transient effects regimes. Indeed, in such burners the recirculation region induces a shear layer which promotes partial premixing of reactants, facilitating combustion. However, the high shear rates may complicate the stabilization of non-premixed flames and cause local extinction of the combustion process.

This paper presents a brief review of the experimental methodology and the mathematical treatment of the measured data. The studied flow fields are compared by analyzing flow similarity, first. The turbulent properties are discussed in detail, with emphasis in the recirculation region.

### 2. METHODOLOGY

Laser diagnostics measurement techniques provide results with high temporal and good spatial resolution. These features are essential to the application of turbulent flows where temporal fluctuations are found. In addition, laser measurements are not intrusive, because they avoid the introduction of probes, allowing to study the flow structure without substantial perturbations.

## 2.1 Experimental measurements

The experiments are performed in the arrangement shown in Fig. 1(a) and the dimensions of the bluff body shown are show in Fig. 1(b) (Cruz, 2013). A circular bluff body of diameter  $D_b = 60 \text{ mm}$  is located concentrically in a duct with diameter  $D_a = 200 \text{ mm}$ , which thus generates an annular wind tunnel. The verticality and alignment of the bluff body is regulated with precision screws located at the base. The ample optical access of this configuration permits a proper application of laser diagnostics. A centrifugal fan *Deltra VC – 400*, with maximum flow rate of  $32.8 \text{ m}^3/\text{min}$  is used to supply air to the experiment. The minimum and maximum air flow generating annular air outlet velocity,  $V_a$ , are of about  $4 \text{ m/s}$  and  $12 \text{ m/s}$ , respectively, corresponding to  $20 - 60 \text{ Hz}$  graduations of frequency inverter that controls the rotation of the fan. The air supply system includes a tranquilizing box and circular perforated grids upstream to the bluff body, intended to provide uniform the flow velocity and generate homogeneous turbulence at output.

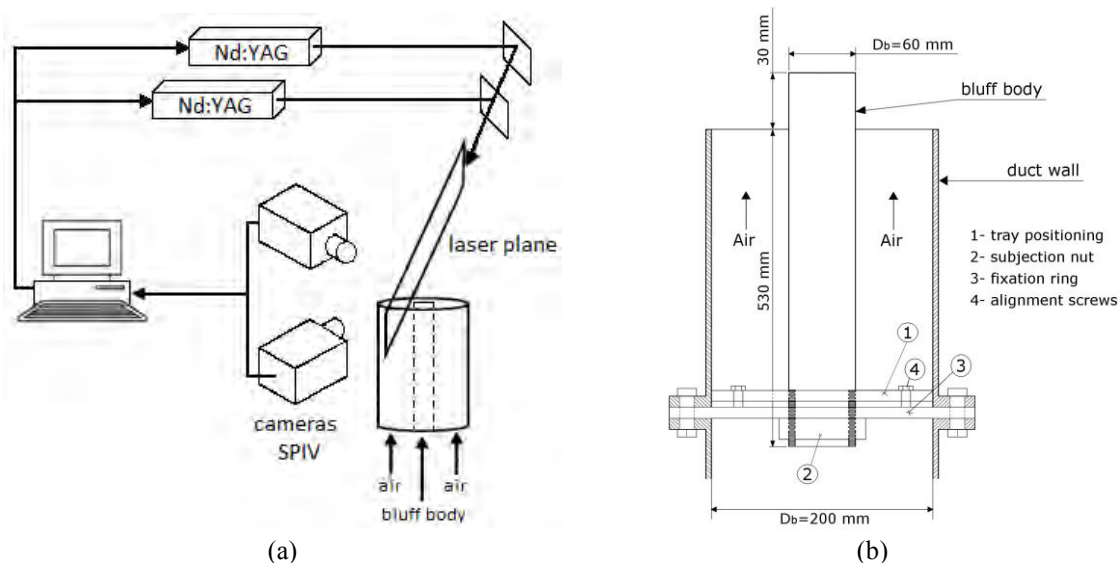


Figure 1 Experimental setup (a) experimental equipment and (b) bluff body dimension.

The Stereo PIV technique (Raffel, *et al.*, 2007) is used to study the different air flow velocities shown in Table 1. The dual laser pulse *Nd: YAG CFR 200*,  $200 \text{ mJ}$  of energy at  $15 \text{ Hz}$ , provides a laser beam at second harmonic ( $\lambda = 532 \text{ nm}$ ), which is transformed into a plane of  $0.5 \text{ mm}$  average thickness using a set of cylindrical lenses. The time between laser pulses,  $dt$ , is adjusted according to Table 1, in order to restrict the displacement of the particles to  $8 \text{ px}$ . All the walls of the annular duct and bluff body have been painted black to reduce laser scattering captured at the images. The image recording is made with two *Image Intense* cameras of *LaVision* with  $1376 \times 1040 \text{ px}^2$  CCD and  $10 \text{ Hz}$  of maximum capture rate. *DAVIS 7.2* software is used to control the trigger signal of lasers and cameras. Titanium oxide ( $\text{TiO}_2$ ) tracer particles are homogeneously uniformly seeded in the air flow using cyclone combined with a fluidized bed, thus providing particles with an average diameter of  $1.0 \mu\text{m}$ . This particle diameter ensures a good light scatter and follows the flow fluctuations at the entire measurement field (Caetano, 2012; Novgorodcev, 2012). The cameras are arranged at an angle of  $35^\circ$  and oriented towards the same side of the laser plane. The measurement region is  $140 \times 105 \text{ mm}^2$  is located downstream to the bluff body surface and centered on its symmetry line, thus leading to a  $0.1 \text{ mm/px}$  image resolution. The particle displacement fields are obtained by applying multi-pass decreasing window size of  $64 \times 64$  to  $32 \times 32$  pixels in two passes, with parameters overlap of  $50\%$ , resulting in a spacing of  $1.63 \text{ mm}$  between vectors. The Whitaker reconstruction method is employed to achieve accurate sub-pixel displacement resolution. Finally, average velocity fields,  $V_i$ , and Reynolds stresses,  $R_{ij}$ , result from processing 1000 pairs of instantaneous images for each studied case.

Table 1 Operating parameters of the studied cases ( $\delta V_a/V_a=3.0\%$ ;  $\delta Re/Re_a = 4.36\%$ ).

Case	$V_a \text{ [m/s]}$	$Re$	$dt \text{ [\mu s]}$
1	4,0	15000	110
2	8,0	30000	56
3	11,8	45000	39

## 2.2 Mathematical treatment

In this work, the turbulent flow is analyzed, first, by studying the average velocity and the Reynolds stress components fields. Then are discussed properties derived from these fields, i.e., the strain rate  $S_{xy}$  and vorticity  $W_{xy}$  components.

$$S_{xy} = \frac{1}{2} \left( \frac{\partial V_x}{\partial x} + \frac{\partial V_y}{\partial y} \right) ; \quad W_{xy} = \frac{1}{2} \left( \frac{\partial V_x}{\partial x} - \frac{\partial V_y}{\partial y} \right). \quad (1)$$

Further characterization of the turbulent state is achieved through the theory of Lumley (Lumley, 1978), which involves the anisotropy tensor ( $b_{ij}$ ) and the associated invariants ( $I_n$ ). The anisotropy tensor can be defined as:

$$b_{ij} = \frac{R_{ij}}{k} - \frac{2}{3} \delta_{ij}, \quad (2)$$

where  $R_{ij}$  are the Reynolds tensor components and  $\delta_{ij}$  Kronecker delta (Pope, 2000). The anisotropy  $b_{ij}$  is a zero trace tensor and, hence, has only two independent invariants, the traces of  $b_{ij}^2$  and  $b_{ij}^3$  matrices, i.e.,  $II = b_{ij}b_{ji}$  and  $III = b_{ij}b_{jk}b_{ki}$ , respectively. The classical graphical representation of the turbulent states involves  $(III, -II)$  coordinates. It may be shown that the realizable region is a triangle, which is shown in Fig. 2. Inside this triangle are situated all possible values of the invariants and its boundaries match particular turbulent states. This allows characterizing the turbulent states by means of invariants only. Furthermore, in order to estimate the local degree of departure from isotropy, the parameter  $R$  (Hartmann, *et al.*, 2004) may also be used:

$$R = \sqrt{(III)^2 + (-II)^2}, \quad (3)$$

which may be interpreted as the degree of deviation from the isotropic state ( $R = 0$ ).

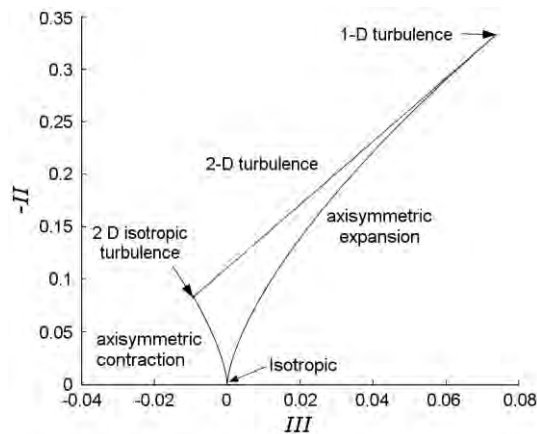


Figure 2 Lumley triangle showing the possible turbulence states.

## 3. RESULTS AND DISCUSSION

### 3.1 Average velocity field

Figure 3 shows the average field of the velocity component in the main flow direction,  $V_y$ , and the corresponding flow structure. In Fig. 3(a), streamlines are superimposed on the average velocity field (left half) and the velocity vectors are given at the other half. Note the air flow convergence toward a stagnation point the centerline ( $x = 0$ ), which limits a recirculation zone between the face of the bluff body. The streamlines clearly show the formation of an axisymmetric toroidal vortex. Figure 3(b) shows a scheme of the global structure of the flow. The recirculation zone extends from the face of the bluff body to the stagnation point and around the toroidal vortex. It is also possible distinguish a zero velocity surface,  $V_y = 0$ , which delimits a region where negative values of  $V_y$  are found only.

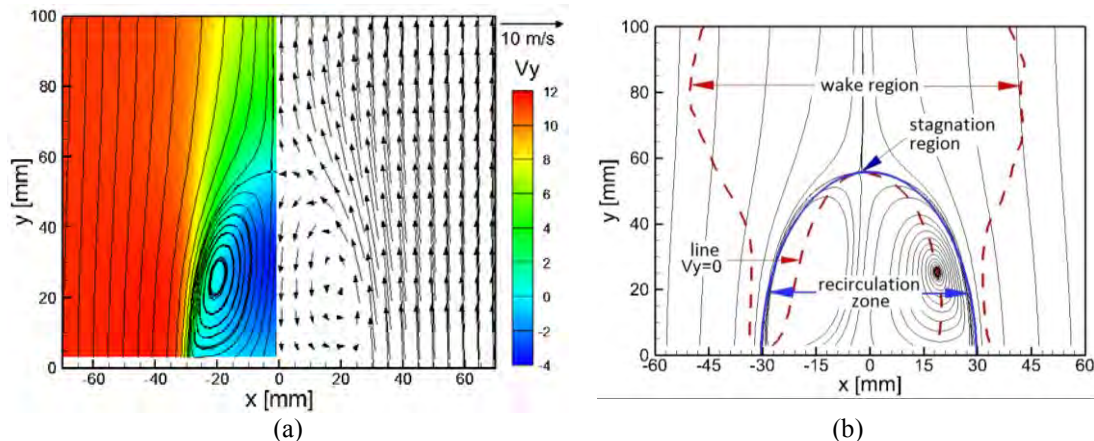


Figure 3 Flow structure (a) Average longitudinal velocity component field,  $V_y$ , streamlines and velocity vectors for case 3 and (b) Mean flow structure.

The different flow velocities studied exhibit similarity in the mean velocity and Reynolds tensor fields. Indeed, the deviations observed are smaller than 4.0 %, when the velocity values are normalized by  $V_{y,max}$ , the Reynolds stresses by  $V_{y,max}^2$  and all distances are normalized by the bluff body diameter. This can indeed be observed in Fig. 3(a), which shows the longitudinal velocity component,  $V_y$ , along the centerline ( $x = 0$ ),  $D_b = 60$  mm. It is evident that velocity displays negative values first decreasing to a point at  $y/D_b \approx 0,45$  and, then, increases to the stagnation point located at  $y/D_b \approx 0,92$ . Henceforth are analyzed result of case 3, only, corresponding to the highest Reynolds number. Also can be seen in Fig. 4(b), that the vortex center is always located at the line  $x/D_b \approx -0,33$ , and height  $y/D_b \approx 0,45$  downstream to the bluff body face.

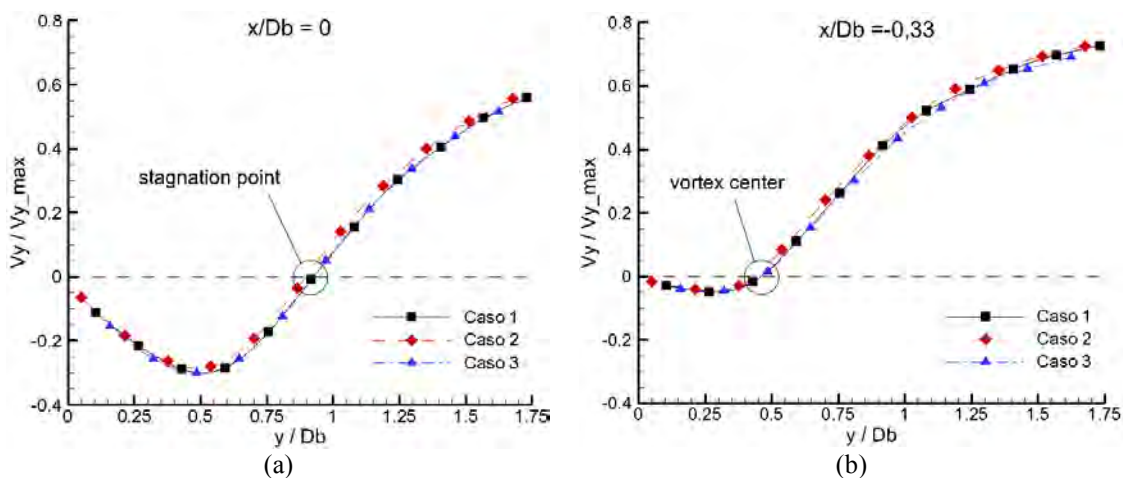


Figure 4 Longitudinal evolution of the average velocity component  $V_y$  (a) centerline  $x/D_b = 0$  and (b) row  $x/D_b = -0,33$ ; i.e., passing through of the vortex center.

In Fig. 5, where are shown the normalized average longitudinal and transversal velocity components, a typical wake zone behavior may be observed. An overall pattern of good symmetry with respect to the centerline ( $x/D_b = 0$ ) is observed for both components with discrepancies smaller than 3.5 %. Also,  $V_x$  is zero at the center line and subject to equally weighted influence of either side of the vortex. The highest  $V_x$  values are attained near the outer edge of the recirculation zone, representing a region of higher air entrainment toward the centerline. This general trend is broken only at  $y/D_b = 0.17$ ,  $|x/D_b| \leq 0,5$ , where the flow is directed toward the rim of the bluff body, since this line crosses the bottom part of the vortex. For  $|x/D_b| > 0,5$ , air entrainment toward the centerline is always observed. Concerning the longitudinal velocity component,  $V_y$ , an abrupt velocity decrease is found at the bluff edge  $|x/D_b| \approx 0,5$ , thus generating a region of intense shear at the recirculation zone vicinity. Negative velocity component values occur at  $y/D_b < 0,9$  mm due to the presence of the recirculation zone. The antisymmetric variation of  $V_x$  is consistent with the  $V_y$  symmetry, due to continuity.

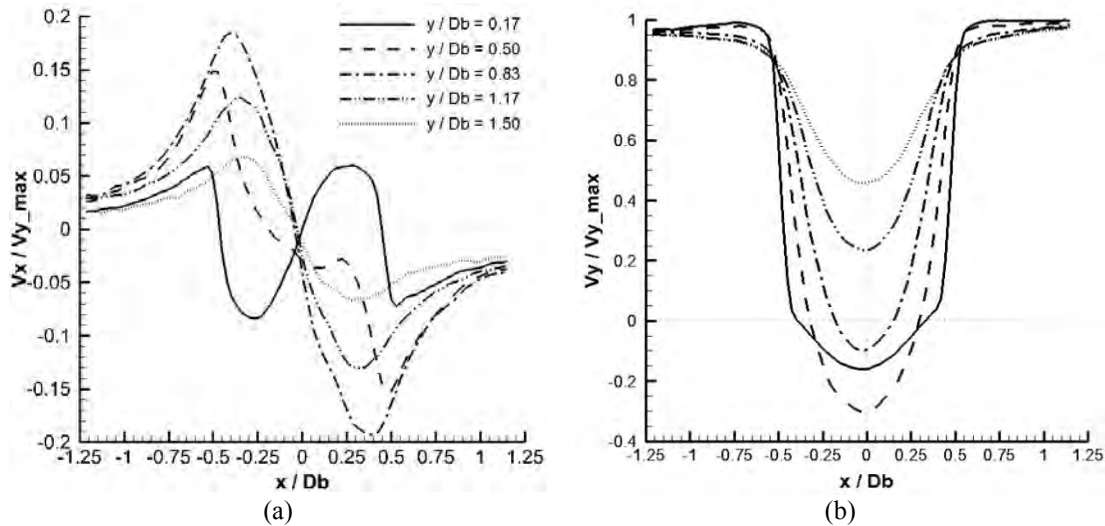


Figure 5 Transversal evolution of the average velocity components, at different heights above the bluff body (a)  $V_x/V_{y\_max}$  and (b)  $V_y/V_{y\_max}$ .

Figure 6 shows that the perpendicular velocity component,  $V_z$ , exhibits a symmetrical behavior and values of same the order of magnitude as  $V_x$ . This behavior is consistent with the fact that,  $V_z$ , is not an angular, but a Cartesian velocity component, which may easily be shown, by invoking continuity, to exhibit a parabolic behavior with  $x$  near  $x = 0$ . Furthermore, the  $V_x < 0$  at  $x = 0$  is also consistent with the negative measured values of  $V_x$  at  $x = 0$ , which underscore a slight flow asymmetry.

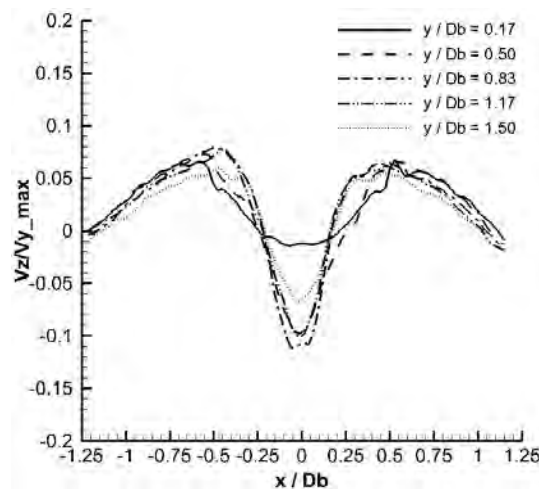


Figure 6 Transversal evolution of the average velocity component  $V_z/V_{y\_max}$  in case 3, at different heights above the bluff body.

### 3.2 Reynolds stress components fields

The normal components of the Reynolds tensor,  $R_{ii}$ , and the main cross component,  $R_{xy}$ , are shown in Fig. 6. For  $|x/D_b| > 0.6$  almost constant values are observed,  $R_{xx}/(V_{y\_max})^2 = 0.5$ ,  $R_{yy}/(V_{y\_max})^2 = 0.7$  and  $R_{zz}/(V_{y\_max})^2 = 1.0$ , which represents an area that could nearly be considered of isotropic turbulence. The measurement results indicate that the turbulent intensity at  $|x/D_b| = 0.75$  and  $y/D_b = 0.17$  is  $I_t = 8.7\%$  (for cases 1 and 2  $I_t = 8.7\%$  and  $8.4\%$  respectively).

Concerning  $R_{ii}$ , reasonable symmetry with respect to centerline is observed, i.e., asymmetry is smaller than 15%. The normal components are not uniform throughout the wake region, indicating that the turbulence structure is anisotropic. The normal components  $R_{xx}$  and  $R_{zz}$  have similar distribution and values, which could have been expected due to burner symmetry. The cross stress  $R_{xy}/(V_{y\_max})^2$  is zero at the symmetry line, as it could have been expected.

Reminding that the derivatives  $-\partial R_{xy}/\partial x$  and  $-\partial R_{yy}/\partial y$  are present in the Reynolds averaged transport equation of longitudinal momentum as turbulent diffusion terms, from Fig. 6d it can be seen that the highest values  $-\partial R_{xy}/\partial x$  are present in the wake region  $0.3 < |x/D_b| < 0.55$ . The derivative  $-\partial R_{yy}/\partial y$  is practically zero in the wake region

and, thus, not predominant for turbulent transport. The cross components  $R_{xz}$  and  $R_{yz}$  exhibit very small values when compared to the others and are not shown here for the sake of brevity. Note, though, that null values of are found in the annular region with a maximum of 0.6% of  $(V_{y\_max})^2$  at recirculation region, indicating a very low degree of correlation between fluctuations of  $V_z$  and others.

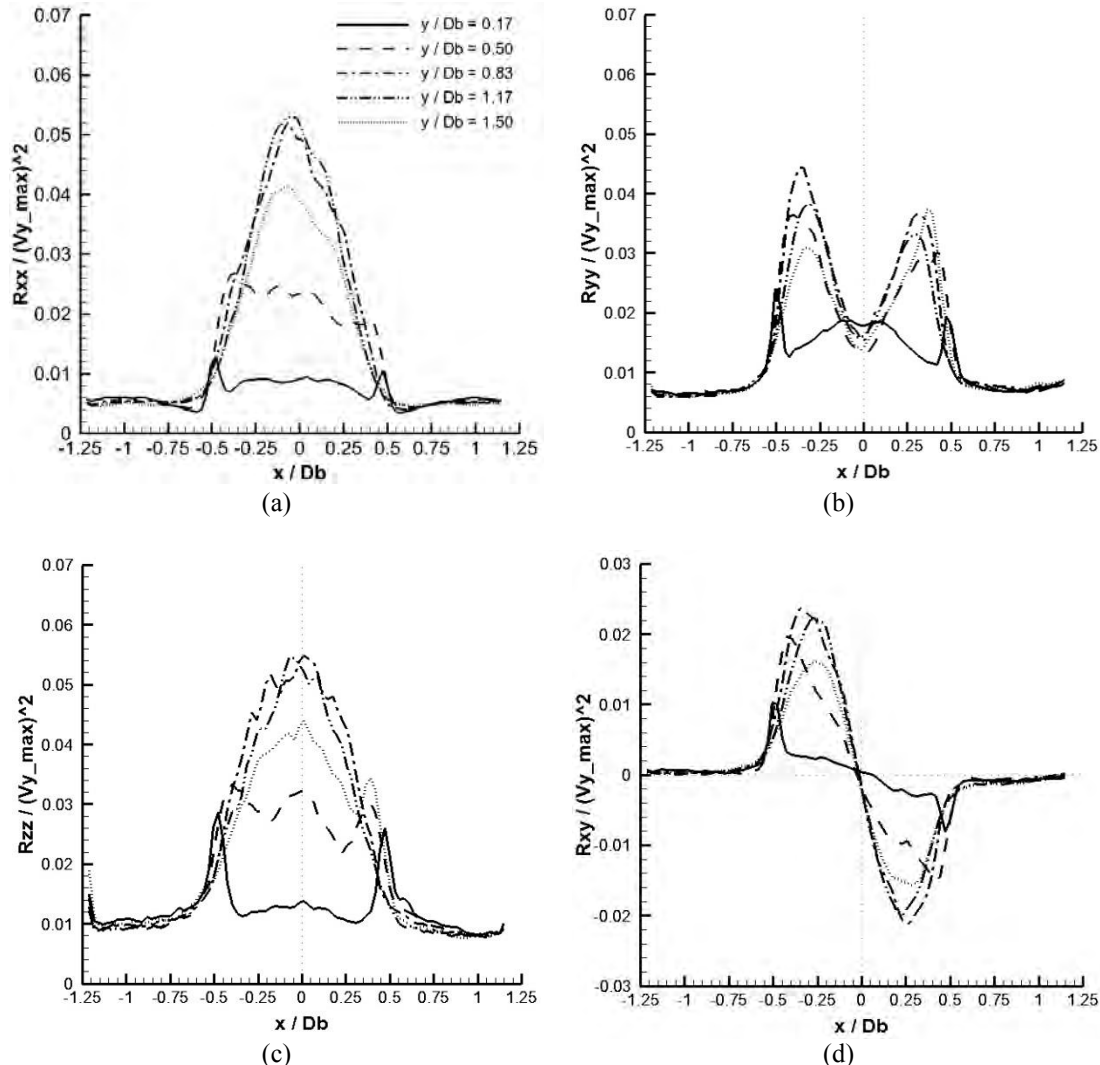


Figure 7 Transversal evolutions of the Reynolds stress components in case 3, at different heights above the bluff body (a)  $R_{xx}/(V_{y\_max})^2$ , (b)  $R_{yy}/(V_{y\_max})^2$ , (c)  $R_{zz}/(V_{y\_max})^2$  e (d)  $R_{xy}/(V_{y\_max})^2$ .

### 3.3 Derived properties

Figure 8 shows the of strain rate  $S_{xy}$  and vorticity tensors  $W_{xy}$  components distributions. Similar distributions and very close values are observed, since that velocity derivative,  $V_x$ , in the main direction,  $y$ , is an order of magnitude smaller than velocity derivative of  $V_y$  in the transversal direction ( $x$ ). These properties both show a configuration of two antisymmetric lobes involving the toroidal vortex. A maximum absolute value of  $S_{xy} = 800 \text{ s}^{-1}$  is found, which is associated to the intense shear layer that originates at the base of the bluff body, as seen in Figure 6. Note that for the applications that are of interest to the authors, these high shear rates may simultaneous increase fuel air mixing and prevent non premixed combustion stabilization (Cruz, 2013).

The  $R$  (Eq. 3) value, shown in Fig. 9, reveals that the edge of the wake and the centerline are more anisotropic flow regions than the annular flow or than the “U” shaped feature. The high anisotropy seems to be related the large longitudinal strain rate at the bluff body rim. Concerning the centerline, Fig. 10, which depict the invariants values sheds some light on the turbulent flow behavior. Indeed, the points corresponding to the annular region ( $x/D_b = -1$ ) show an axisymmetric expansion behavior ( $III > 0$ ). In this figure it may be seen that along  $x/D_b = 0$ , as the flow leaves the stagnation point at  $y/D_b = 0.92$ , the anisotropy decreases with values  $III \approx 0$ , until  $y/D_b = 0.35$ , when isotropy is achieved. From this height to the stagnation point ( $y = 0$ ) anisotropy grows, however as an axisymmetric

contraction ( $III < 0$ ). In the centerline ( $x/D_b = 0$ ), the maximum anisotropy occurs at the vicinity of stagnation points located at  $y/D_b = 0$  and  $0.35\text{ mm}$ . The U-Shaped region, where  $R$  is minimal, seem to be related to streamline divergence. This point is currently under investigation.

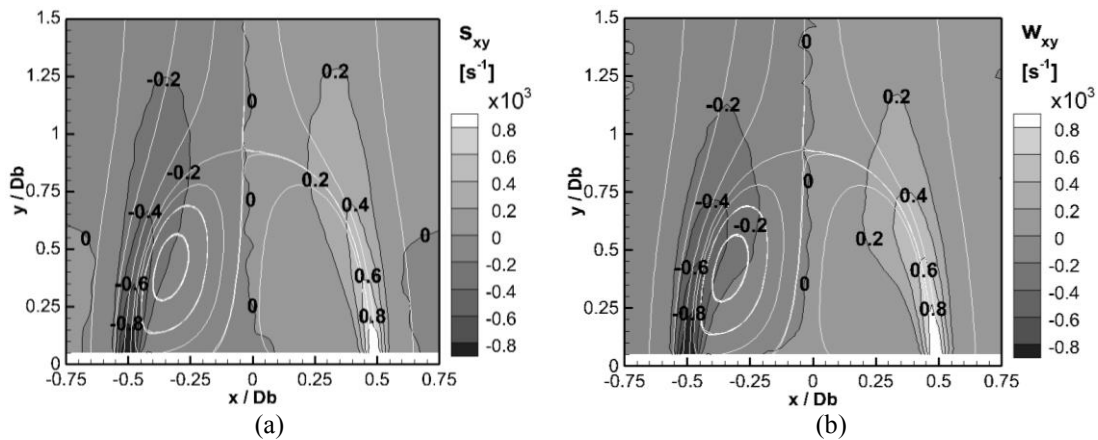


Figure 8 Tensor components of (a) strain rate  $S_{xy}$  and (b) vorticity  $W_{xy}$ .

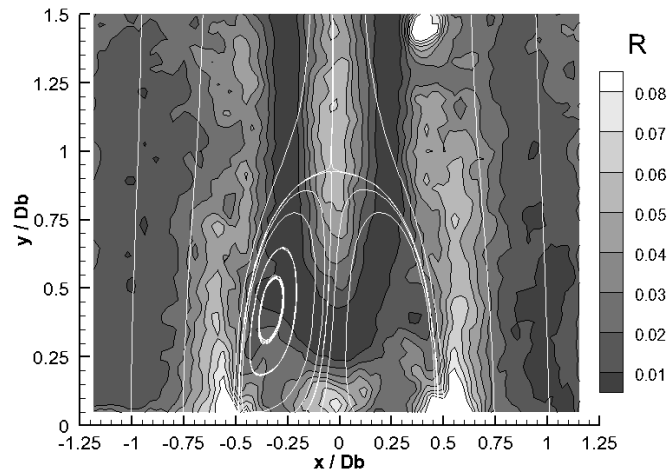


Figure 9 Field of the  $R$  parameter and streamlines, in white.

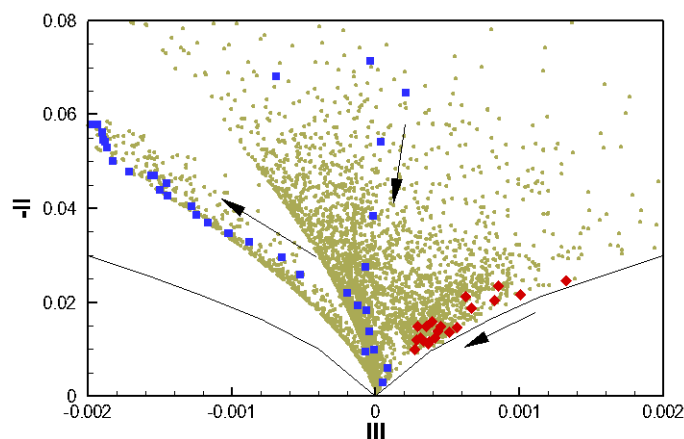


Figure 10 Lumley invariants field ( $\bullet$ ) and longitudinal evolution of the tendency to isotropy of ( $\blacksquare$ )  $x/D_b = 0$  and ( $\blacklozenge$ )  $x/D_b = -1$ .

#### 4. CONCLUDING REMARKS

The measurement results confirmed the existence of similarity between the turbulent flow formed at different Reynolds numbers in the recirculation zone, which includes a toroidal vortex located between the face of the burner and stagnation point ( $y/D_b \approx 0.92$ ) on the center line. The increase of the Reynolds number does not lead to appreciable changes in the velocity and Reynolds stress fields, which is in agreement with previous work (Huang and Lin, 2000).

Juan José Cruz Villanueva, Luís Fernando Figueira da Silva  
 Experimental Study of the 3-D Turbulent Velocity Field Downstream a Bluff Body

Higher intensities of turbulent fluctuations were found in the wake region and the distributions of Reynolds tensor components indicate turbulence anisotropy. For the case of higher Reynolds numbers, the distribution of average strain rate showed a maximum shear on the order of  $800 \text{ s}^{-1}$  in the regions adjacent to the edge of the burner. This is beneficial for mixing processes. The distribution of the average strain rate indicate that the turbulent viscosity models based on the Boussinesq hypothesis should be inappropriate for calculating the Reynolds stress tensors for this type of flow. An analysis of the anisotropy of the tensor Reynolds components employing the Lumley theory further demonstrates anisotropic turbulence behavior.

## 5. ACKNOWLEDGEMENTS

This research has been supported by Capes/Pro-Engenharias and Petrobras. During this work Luís Fernando Figueira da Silva was on leave from the Institut Pprime (Centre National de la Recherche Scientifique, France).

## 6. REFERENCES

- Alva, L. E., 2008. *Caracterização numérica e experimental de uma chama turbulenta não pré-misturada*, Master's thesis, Pontifícia Universidade Católica do Rio de Janeiro, Rio de Janeiro.
- Braza, M., Perrin, R. and Hoarau, Y., 2006. "Turbulence properties in the cylinder wake at high Reynolds number". *Journal of Fluids and Structures*, Vol. 22, p. 757-771.
- Caetano, N. R., 2012. *Estudo Experimental de Chamas Turbulentas não pré-misturadas empregando simultaneamente as técnicas de diagnóstico laser, PLIF e PIV*, Ph.D. thesis, Pontifícia Universidade Católica do Rio de Janeiro, Rio de Janeiro.
- Cruz, J. J., 2013. *Estudo experimental da combustão turbulenta de sprays de etanol usando PLIF-OH, PIV e Shadowgraphy*, Master dissertation, Pontifícia Universidade Católica do Rio de Janeiro, Rio de Janeiro.
- Durao, D. and Whitelaw, J., 1978. "Velocity characteristics of the flow in the near wake of a disk". *Journal of Fluid Mechanics*, Vol. 2, p. 369-385.
- Hartmann, H., Derksen, J., Montavon, C., Pearson, J., Hamill, I. and van den Akker, H., 2004. "Assessment of larger eddy and RANS stirred tank simulations by means of LDA". *Chemical Engineering Science*, Vol. 59, p. 2419-2432.
- Huang, R. and Lin, C., 2000. "Velocity field of a bluff-body wake". *Wind Engineering and Industrial Aerodynamics*, Vol. 85, p. 31-45.
- Kähler, C., 2011. "High-repetition-rate PIV investigations on a generic rocket model in sub- and supersonic flows". *Experiments in Fluids*, Vol. 50, p. 1019-1030.
- Lumley, J., 1978. "Computational modelling of turbulent flows". *Advances in Applied Mechanics*, Vol. 18, p. 123-176.
- Novgorodcev, A., 2012. *Estudo numérico e experimental da combustão turbulenta não pré-misturada de um jato de hidrogênio e ar*, Master's thesis, Pontifícia Universidade Católica do Rio de Janeiro, Rio de Janeiro.
- Pope, S. B., 2001. *Turbulent Flows*. Cambridge University Press, United Kingdom, 1<sup>ra</sup> edition.
- Raffel, M., Willert, C., Wereley, S. and Kompenhans, J., 2007. *Particle Image Velocimetry: A Practical Guide*. Springer, Berlin, 2<sup>da</sup> edition.